Int. J. Heat Mass Transfer. Vol. 35, No. 9, pp. 2219–2232, 1992
Printed in Great Britain

0017–9310/92 $5.00+0.00
Pergamon Press Ltd

Performance of a multigrid three-dimensional magnetohydrodynamic generator calculation procedure

J. X. BOUILLARD and G. F. BERRY
Argonne National Laboratory, 9700 South Cass Avenue, Argonne, IL 60439-4815, U.S.A.

(*Received* 17 *October* 1990 *and in final form* 16 *August* 1991)

Abstract—The formulation and evaluation of a recently developed multigrid finite difference calculation procedure for steady three-dimensional magnetohydrodynamic (MHD) flows are described. This procedure solves, in primitive variables, the parabolized steady-state MHD equation set, which consists of the mass continuity equation, three momentum equations, the energy equation, the turbulent kinetic energy and dissipation rate equations, and Maxwell's equations using a full approximation storage block implicit multigrid finite difference technique. This new technique is first validated by comparing predicted results with experimental data for supersonic and subsonic Faraday generators. The performance of this technique is then assessed in terms of computational speed and solution accuracy. It is shown that the resolution of Maxwell's elliptical electrical equations is computationally speed limiting. A global improvement factor of 3–5 is obtained by using the multigrid finite difference solution procedure.

1. INTRODUCTION

THE INTERACTION of a magnetic field with an electrically conducting gas in magnetohydrodynamic (MHD) generators produces flow phenomena that are inherently three-dimensional in nature. These three-dimensional effects manifest themselves in many forms: velocity overshoots in the boundary layers, flow asymmetries produced by secondary flows, and distorted temperatures and current fields. Much progress in predicting three-dimensional hydrodynamic and electric effects in MHD generators has already been made by several investigators [1–8]. These authors have successfully developed, tested, and validated single-grid three-dimensional MHD computational techniques and computer codes for these types of flows. Although these computer codes are useful and powerful, they are slow in execution. Accurate solution of practical three-dimensional MHD flows is usually expensive in computer time and storage requirements because many computational nodes are necessary for establishing grid-independent solutions.

The purpose of this paper is to describe the formulation and the evaluation of a recently developed, efficient, multigrid finite difference calculation procedure for steady three-dimensional MHD flows. This procedure solves the parabolized steady-state MHD equation set, which consists of the mass continuity equation, three momentum equations, the energy equation, the turbulent kinetic energy and dissipation rate equations, and Maxwell's equations using a full approximation storage (FAS) block implicit multigrid method (BLIMM).

2. MHD MODEL

2.1. *Hydrodynamic model*

Flow phenomena in MHD channels can be represented by the three-dimensional Navier–Stokes equations. Since this flow is predominantly along the axial direction, certain simplifications can be made by consideration of the order of magnitude of various terms. The simplification made here is referred to as the parabolic approximation [9, 10]. Because the flow velocities in the channel are high, the effects of turbulence must be accounted for. In the present paper, a two-equation (k–ε) model is used, and the turbulent fluxes are represented as the product of turbulent viscosity and the gradients of the flow variables (Tables 1 and 2).

The turbulent viscosity is calculated from the local values of turbulent kinetic energy (k) and its dissipation rate (ε), using the following formula:

$$\mu_t = \rho C_\mu \frac{k^2}{\varepsilon}. \tag{1}$$

The different values of the constants used in the turbulent model are presented in Table 3.

In addition, because of steep near-wall gradients,

Table 1. Magnetohydrodynamic model

$\text{div}\,(\rho \mathbf{U}\phi - \Gamma^\phi \,\text{grad}\,\phi) = S^\phi$	(T1)
$\text{rot}\,\mathbf{E} = 0, \quad \text{div}\,\mathbf{J} = 0$	(T2)
$\mathbf{J} = \sigma(\mathbf{E}+\mathbf{U}\times\mathbf{B}) - (\beta/B)\mathbf{J}\times\mathbf{B}$	(T3)

NOMENCLATURE

B, B^k magnetic field [T], right-hand side of equation (21) on grid k
c electrode width [m]
C_1, C_2, C_μ constants in the turbulence model
D dissipation term in enthalpy equation [W m^{-3}]
e_k norm error on grid k
E_r constant in wall function
E_0 value of E at zero roughness
$\mathbf{E}$ electric field vector [V m^{-1}]
E_x, E_y, E_z components of $\mathbf{E}$
ERCONT continuity equation normalized residuals
ERPOT electric potential residuals of equations (9)
G generation of turbulence energy [W m^{-3}]
h static enthalpy [J kg^{-1}]
H channel height (distance between electrode walls) [m]
I prolongation or restriction operator
I_l load current [A]
J_x, J_y, J_z current components in x, y, and z directions [A m^{-2}]
J current vector
k turbulent kinetic energy [J kg^{-1}]
K load factor
L elliptic operator
p static pressure [Pa]
p_i electrode pitch [m]
$\tilde{p}$ pressure field in axial momentum equation [Pa]
P_r heat transfer resistance of laminar sublayer
P_0 value of P_r at zero roughness
Q_w wall heat flux [W m^{-2}]
R_l external load resistance [Ω]
R_r roughness Reynolds number
S^ϕ source term for the flow variable ϕ
t time [s]
T temperature [K]
$\mathbf{U}$ velocity vector
u, v, w components of velocity vector in x, y, and z directions [m s^{-1}]
w^k, W^k solution vector in the multigrid algorithm
W width of channel cross-section
x, y, z coordinate directions [m]
y_r equivalent roughness height [m].

Greek symbols
β Hall parameter
γ diagonalization angle [deg]
Γ^ϕ generalized diffusion coefficient in equation (1) in Table 1
δ tolerance adjustment factor
ε dissipation rate of turbulence energy [W kg^{-1}], tolerance residual on grid k
η cross-section electrical potential [V]
η_1, η_2 components of η after decomposition [m, V respectively]
κ Von Karman's constant used in the wall function
μ_t turbulent viscosity [kg m^{-1} s^{-1}]
μ_l laminar viscosity [kg m^{-1} s^{-1}]
ρ fluid density [kg m^{-3}]
σ_l laminar Prandtl number
σ_h, σ_k, σ_ε turbulent Prandtl numbers for h, k, and ε
σ electric conductivity [S m^{-1}]
σ_n $\sigma/(1+\beta^2)$
τ shear stress [Pa]
ϕ flow variable
ψ electrical potential [V].

Subscripts
l laminar, electrical load
new new values in an iteration scheme
old old values in an iteration scheme
p first nodal point away from the wall
t turbulent value
w wall
x, y, z x, y, and z direction values.

Superscripts
c variable value on coarse grid
f variable value on fine grid
k intermediate grid level
M finest grid level
T transpose of a tensor
ϕ dependent variable in differential equation.

Operators
∇ gradient
$\nabla\cdot$ divergence
$\langle\ \rangle$ cross-section average.

wall functions must be used at the near-wall nodes. Wall functions are necessary to avoid using very fine grids near the wall [11]. Based on the assumption that a logarithmic velocity profile prevails in the region between the wall and the near-wall node P, the axial velocity and the wall shear stress are related by the following expression:

$$\frac{W_p}{\sqrt{(\tau_w/\rho)}} = \frac{1}{\kappa}\ln\left(\frac{E_r y_p \sqrt{(\tau_w \rho)}}{\mu_l}\right) \tag{2}$$

where the subscript p indicates that the values are those at grid node P, and the subscript w indicates the values at the wall; y_p is the distance from the wall, and κ and E_r are the log-law constants ($\kappa = 0.4$ and

Table 2. Diffusion coefficients and source terms for equations in Table 1 in the x, y, z coordinate system

Equation	ϕ	Γ^ϕ	S^ϕ
Continuity	1	0	0
Momentum	u	$\mu_l+\mu_t$	$-\frac{\partial p}{\partial x}$
	v	$\mu_l+\mu_t$	$-\frac{\partial p}{\partial y}-J_z B$
	w	$\mu_l+\mu_t$	$-\frac{\partial \bar{p}}{\partial z}+J_y B$
Enthalpy	h	$\frac{\mu_l}{\sigma_l}+\frac{\mu_t}{\sigma_t}$	$u\frac{\partial p}{\partial x}+v\frac{\partial p}{\partial y}+w\frac{\partial \bar{p}}{\partial z}+\frac{J^2}{\sigma}+D$
Turbulent energy	k	$\mu_l+\frac{\mu_t}{\sigma_k}$	$G-\rho\varepsilon$
Turbulent Dissipation rate	ε	$\mu_l+\frac{\mu_t}{\sigma_\varepsilon}$	$C_1 G\varepsilon/k-C_2\rho\varepsilon^2/k$

$D=(\tau_l+\tau_t)\colon\ \nabla\mathbf{U}$, $G=\tau_t\colon\ \nabla\mathbf{U}$, $\tau_l=\mu_l(\nabla\mathbf{U}+\nabla\mathbf{U}^T)$, $\tau_t=\mu_t(\nabla\mathbf{U}+\nabla\mathbf{U}^T)$.

Table 3. k-ε model constants

C_μ	C_1	C_2	σ_k	σ_ε	σ_h
0.09	1.44	1.92	1.0	1.3	0.9

$E_r=E_0=8.12$); W_p is the resultant velocity at P and is assumed to be parallel to the wall shear stress. The node P is chosen so that the local turbulent Reynolds number $(\rho\sqrt{k}y/\mu_l)_p$ is much greater than unity.

Note that no provision for turbulence damping effects by magnetic fields is given in the turbulence modeling presented in Table 2. The shear stress in the fluid layer between the node P and the wall is then related to the turbulent kinetic energy because, in the uniform-shear-stress layer, the generation and dissipation of k are nearly in balance. This leads to the following relation:

$$\tau_p=\tau_w=\rho\sqrt{C_\mu}k_p. \tag{3}$$

The rate of dissipation of kinetic energy ε_p near the wall is fixed by the requirement that the length scale varies linearly with distance from the wall; the corresponding expression for ε_p is then given by [6]

$$\varepsilon_p=C_\mu^{3/2}k_p^{3/2}/(\kappa y_p) \tag{4}$$

where k_p is the near-wall turbulent kinetic energy. The quantity k_p is calculated from the regular balance equation, but with the following changes. First, the diffusion of turbulent kinetic energy is set equal to zero. The generation term in the kinetic energy equation is then modified to account for the value of wall shear stress calculated using equation (3). The dissipation term is also modified in light of equation (4), and is assigned an average value over the control volume for the near-wall node. Thus,

$$\bar{\varepsilon}=\frac{1}{y_c}\int_0^{y_c}\varepsilon\,dy \tag{5}$$

where y_c is the distance between the edge of the control volume and the wall.

The wall functions for the transport of temperature (or enthalpy) are derived in a manner similar to equation (2). The near-wall variation of enthalpy is also assumed to be logarithmic, the expression being

$$\frac{h_w-h_p}{Q_w}\sqrt{(\tau_w\rho)}=\frac{\sigma^t}{\kappa}\ln\left(\frac{E_r y_p\sqrt{(\tau_w\rho)}}{\mu_l}\right)+P_r \tag{6}$$

where τ_w is given by equation (3), Q_w represents the convection heat flux from the wall, and h represents the static enthalpy. The term P_r (absent in equation (2)) represents the additional resistance to the transfer of heat caused by the existence of the laminar sublayer (from Launder and Spalding [11]).

The values of P_r and E_r are modified to account for rough surfaces. In the approach followed here (recommended by Jayatillaka [12]), the constants E_r and P_r are related to the equivalent sand grain roughness [6, 13].

2.2. *Electrical model*

The complete steady-state three-dimensional finite segmentation solution of the electrical field, the potential, and current densities for an MHD generator requires an elliptical three-dimensional calculation procedure, which is usually slow and requires a large computer memory.

The effects of finite segmentation on the global performance of MHD generators become negligible for medium or large base load generators that have a pitch-to-height ratio of the order of 1–5% [14, 15]. For smaller generators, finite segmentation effects become more important and should be considered. For such generators, infinite segmentation analysis usually overpredicts their global performance [15, 16].

In this paper, we present and use the cross-plane infinite segmentation electrical model formulated by Ahluwalia and Vanka [17]. Their model was successfully applied to the three-dimensional analysis of Faraday, diagonal-insulating and diagonal-conducting side-wall MHD generators [6, 14, 16, 17]. This model is coupled to the gas dynamic model as explained below.

The electrical governing equations consist of Maxwell's steady-state equations (equation (T2), Table 1) and Ohm's law (equation (T3), Table 1). Because of the form of equation (T2) in Table 1, it is possible to define an electric potential ψ such that

$$\mathbf{E}=-\nabla\psi. \tag{7}$$

In the following discussion, it is assumed that the magnetic field $\mathbf{B}$ is uniform in the channel cross-section and is oriented along the x direction. Consequently, the vector notation is dropped in the following discussion.

The infinite segmentation model is constructed from equation (T2) in Table 1 by neglecting axial variations of the flow and electrical variables in comparison with their cross-plane variation. Consequently, the Hall electric field E_z is assumed to be constant in a cross-section plane. The electric potential ψ can be expressed as [6, 14–17]

$$\psi = -zE_z + \eta(x, y). \tag{8}$$

The first term in equation (8) represents the contribution of the Hall electric field E_z, and η is the electrical potential in the cross-section plane. Substituting equation (8) into equation (7) and equation (T2) in Table 1 results in the following equation for the two-dimensional function $\eta(x, y)$:

$$\frac{\partial}{\partial x}\left(\sigma\frac{\partial\eta}{\partial x}\right) + \frac{\partial}{\partial y}\left(\sigma_n\frac{\partial\eta}{\partial y}\right) = E_z\frac{\partial}{\partial y}(\beta\sigma_n) - \frac{\partial}{\partial y}[\sigma_n B(w-\beta v)] \tag{9}$$

where $\sigma_n = \sigma/(1+\beta^2)$. Since E_z is not known *a priori*, the following potential decomposition is adopted:

$$\eta(x, y) = E_z\eta_1(x, y) + \eta_2(x, y). \tag{10}$$

The two functions η_1 and η_2 are governed by the following equations:

$$L[\eta_1] = \frac{\partial}{\partial y}(\beta\sigma_n) \tag{11}$$

and

$$L[\eta_2] = \frac{\partial}{\partial y}[\sigma_n B(w-\beta v)] \tag{12}$$

where the elliptical operator L is defined as

$$L = \frac{\partial}{\partial x}\left(\sigma\frac{\partial}{\partial x}\right) + \frac{\partial}{\partial y}\left(\sigma_n\frac{\partial}{\partial y}\right). \tag{13}$$

Note that the function η_1 is driven by the conductivity nonuniformity, and η_2 by both the conductivity and velocity nonuniformities. Both η_1 and η_2 are independent of E_z, which is reduced to a parameter of the problem. This will be determined later from the specification of the external electrical connection and loading. Assuming a Faraday electrical connection, the cross-section averaged Hall current density $\langle J_z\rangle$ is identically zero. Thus, the Hall electric field E_z may be expressed as:

$$E_z = -\frac{\left\langle\sigma_n\beta\dfrac{\partial\eta_2}{\partial y}\right\rangle + B\langle\sigma_n(\beta w+v)\rangle}{\langle\sigma_n\rangle + \left\langle\sigma_n\beta\dfrac{\partial\eta_1}{\partial y}\right\rangle}. \tag{14}$$

The current densities J_x, J_y, and J_z are calculated using Ohm's law (equation (T3), Table 1).

3. BOUNDARY AND INLET CONDITIONS

Boundary conditions for the functions η_1 and η_2 are defined by the channel configuration. For a Faraday connection, several types of boundary conditions may be used for the potential equation [6, 13]. In this paper, we express the electrical boundary conditions in terms of the external load resistance. The difference of potential $(\eta_H - \eta_0)$ and the cross-section average current density $\langle J_y\rangle$ are related through the external resistance (R_l), the electrode pitch (p_l), and the channel width (W) by

$$\langle J_y\rangle p_l W R_l = \eta_H - \eta_0. \tag{15}$$

From Ohm's law, $J_z + \beta J_y = \sigma(E_z + vB)$, which for a Faraday connection leads to

$$\langle\beta J_y\rangle = \langle\sigma\rangle E_z + \langle\sigma v\rangle B. \tag{16}$$

To obtain decoupled boundary conditions, we assume that in equation (16),

$$\langle\beta J_y\rangle = \langle\beta\rangle\langle J_y\rangle. \tag{17}$$

Combining equations (15), (16), and (17) and noting the arbitrariness in η_0, it follows that

$$\eta_1 = \eta_2 = 0 \quad \text{at} \quad y = 0 \tag{18}$$

$$\eta_1 = \frac{\langle\sigma\rangle}{\langle\beta\rangle} p_l W R_l \quad \text{at} \quad y = H \tag{19}$$

and

$$\eta_2 = \frac{\langle\sigma v\rangle}{\langle\beta\rangle} B p_l W R_l \quad \text{at} \quad y = H. \tag{20}$$

The extent of inaccuracy introduced by the approximation of equation (17) is generally less than 1% of the power density [14]. The external resistance and the electrode pitch are allowed to vary in the axial direction, with their variations specified as input data [13]. The Hall electric field E_z is determined by equation (14). This type of Faraday connection with its associated boundary conditions is presented in Fig. 1.

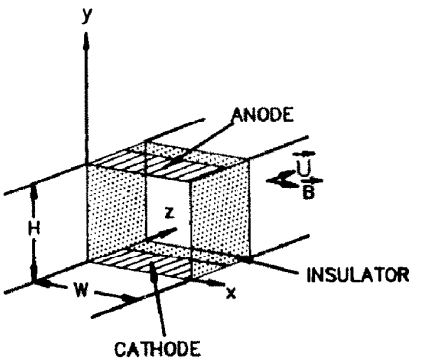

FIG. 1. Schematic of the Faraday generator configuration.

Slip and no-slip boundary conditions can be imposed on the velocity fields. In the case of a no-slip boundary condition at the wall, the law of the wall is used for turbulent flows. In the case of a slip boundary condition (i.e. symmetry), a zero-derivative condition is applied to all scalar variables and tangential velocities. The channel geometry is prescribed through the

specifications of the axial distributions of the channel height and width. Boundary conditions for the energy equations are specified by the imposition of the experimental wall temperature.

4. STATE EQUATIONS

To close the system of fluid dynamic and electrical equations, it is necessary to establish relationships between the fluid properties and the selected solution transport (u, v, w, $\bar{p}$, h). Although several alternatives are possible, in this paper thermodynamic and electrical properties were calculated using the NASA computer code [18] and are curve fitted with fourth-order interpolation polynomials in $\bar{p}$ and h. The ideal gas law was assumed.

5. SOLUTION PROCEDURE

The MHD model presented in Table 1 is solved by using a parabolic marching technique in the axial direction [9] and an elliptic solution procedure in the cross-stream directions. For elliptic equations, faster convergence can be obtained by using multiple grids and continuously cycling the solution on coarse and fine grids. As a result, ANL developed a new multigrid computer code called MGMHD [13]. In this code, the cross-stream plane continuity and elliptic momentum equations are solved simultaneously by an FAS BLIMM algorithm [19, 20], and the cross-stream elliptic potential equations are solved using an FAS multigrid procedure [21]. The main features of the MGMHD computer code are described in the following sections.

5.1. *The multigrid concept*

The concept of the multigrid technique can be explained as follows. Consider a set of linear finite difference equations,

$$L^M W^M = B^M, \tag{21}$$

for a general elliptic operator L (for example, equation (13)), where W is the solution vector. Any iterative procedure such as Gauss–Seidel, Jacobi, or incomplete LU converges rapidly for the first few iterations and very slowly thereafter. A Fourier analysis of the error-reduction process shows that these conventional iterative procedures are most efficient in smoothing out errors of wavelengths comparable to the mesh size, but are inefficient in annihilating low-frequency components. The multigrid technique is based on the premise that each frequency range of error must be smoothed on the grid where it is most suitable to do so. Consequently, the multigrid technique cycles between coarse and fine grids until all frequency components are appropriately smoothed.

The multigrid method cycles between a hierarchy of computational grids D^k with corresponding functions W^k, $k = 1, 2, \ldots, M$. The step size on D^k is h_k and $h_{k+1} = h_k/2$, so that D^k becomes finer as k increases. The solution of equation (21) is ultimately searched on the finest grid $k = M$. The auxiliary coarse grids, $k = 1, 2, \ldots, M-1$ are only used to accelerate the convergence rate of the relaxation procedure (iteration) as explained below. By doubling the mesh size in the x and y directions (see Fig. 2, which shows the full coarsening technique), several levels of auxiliary coarse grids ($k = 1, \ldots, M-1$) are thus generated.

In the FAS procedure, the solution is initialized on the finest grid M (see Fig. 3). When the relaxation procedure (iteration) fails to smooth the residuals at the desired theoretical rate on the finest grid M, the iterations are stopped on grid M and the residuals ($B^M - L^M w^M = R^M$; w^M is an approximation to W^M) are transferred to the next coarser grid (restriction). On the coarser grid D^{k-1}, the equation solved is

$$L^{k-1} w^{k-1} = B^{k-1} + I_k^{k-1}(B^k - L^k w^k) - R^{k-1} \tag{22}$$

where L^{k-1} is the operator on grid D^{k-1}, and I_k^{k-1} is the operator to restrict (project) the k variables on grid $k-1$. If the residuals R^{k-1} of equation (22) do not meet the tolerance level on grid $k-1$, R^{k-1} is restricted to grid $k-2$ and a solution of equation (22) is sought on grid $k-2$. When an accurate solution of equation (22) is obtained, the change from the previous value $w^{k-1} - I_k^{k-1} w_{\text{old}}^k$ is prolongated (bilinear interpolation) to grid k. The correction to w^k is then

$$w_{\text{new}}^k = w_{\text{old}}^k + I_{k-1}^k (w^{k-1} - I_k^{k-1} w_{\text{old}}^k). \tag{23}$$

The iterations on each grid k are continued until the required convergence criterion $|e^k| \leqslant \varepsilon^k$ is met, at which time the solution vector is transferred to the next finer level (ε^k is the tolerance level allowed on grid k). When the finest level is solved to the desired accuracy, the overall solution cycle is terminated.

5.2. *Sequence of calculation steps*

The present procedure offers the economical feature of a three-dimensional parabolic procedure in the sense that only a two-dimensional computer storage is required, even though the flow is three-dimensional and the more general set of equations is elliptic. Consequently, axial and cross-stream momentum equations, as well as the longitudinal and cross-stream pressure gradients, are decoupled.

For simplicity, the hydrodynamic and electrical

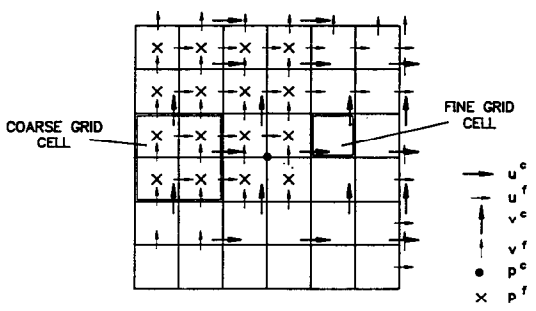

FIG. 2. Staggered arrangement of velocities and pressures in a full coarsening technique.

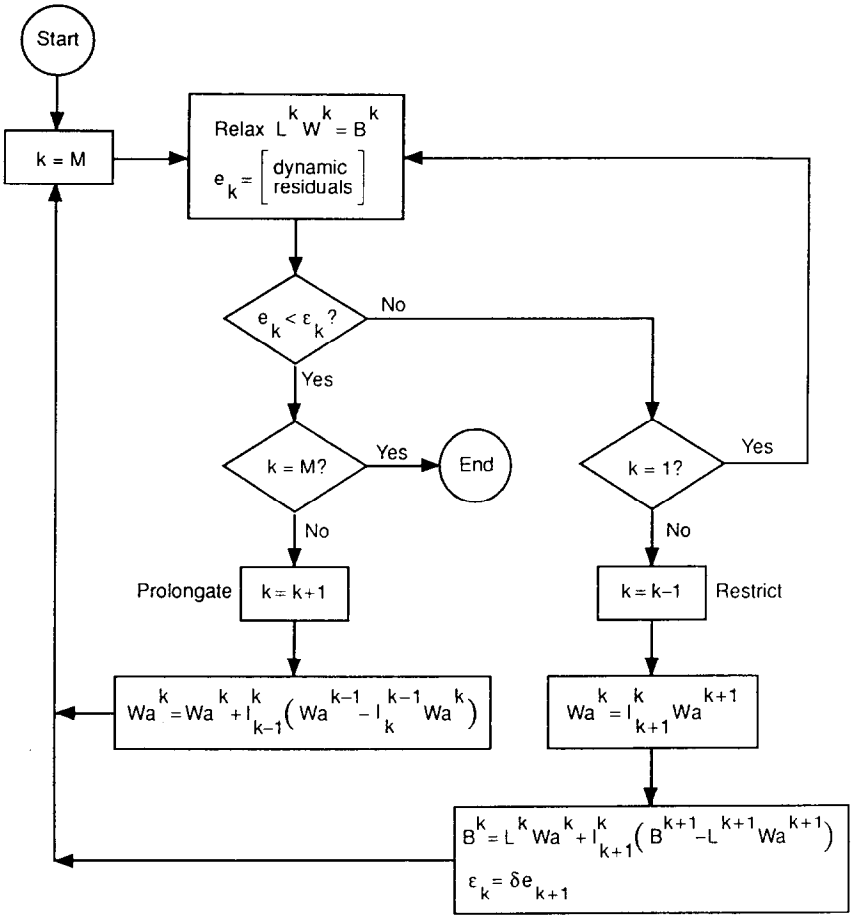

FIG. 3. Flow chart of the multigrid adaptive FAS solution cycle (Wa is an approximation to W).

numerical solution schemes are decoupled. The energy equation is also solved independently since the temperature influences are only propagated through the viscosity and the density, which are kept constant in the iterative solution of the momentum and continuity equations. Since several equations are decoupled from the others, the following sequence is adopted at each axial section until the exit of the channel is reached:

1. New fluid properties are evaluated at the new axial station from the enthalpy and pressure calculated at the previous axial station.
2. The electrical potential equations are solved using an FAS multigrid procedure, and the electric currents and fields are then calculated.
3. The axial momentum equation is solved using the pressure gradient evaluated at the previous axial station with a single-grid Gauss–Seidel point relaxation technique. The axial velocity and pressure gradient are adjusted to satisfy the integral mass-conservation equation.
4. Cross-sectional plane velocity and pressure fields are solved using an FAS BLIMM algorithm [19].
5. The equations for the turbulent kinetic energy, its dissipation rate, and the enthalpy are then solved using a single-grid Gauss–Seidel point relaxation technique.

The cross-section averaged pressure $\bar{p}$ is updated using its value at the previous station and the newly calculated axial pressure gradient (step 3). At the inlet station, variables are initialized with specified values.

6. PROCEDURE VALIDATION: COMPUTATIONAL RESULTS AND COMPARISON WITH EXPERIMENTAL DATA

The MGMHD computer code was developed to predict the three-dimensional flow and electrical performances of several Faraday and diagonal generators. Two simulations, for supersonic and subsonic Faraday generators, are briefly reported in this paper. Reference [13] presents detailed information on these simulations. The purpose of these two examples of Faraday generator calculations is to show that the calculation procedure is adequate to represent the main characteristics of Faraday generators. The computational performance of the multigrid technique

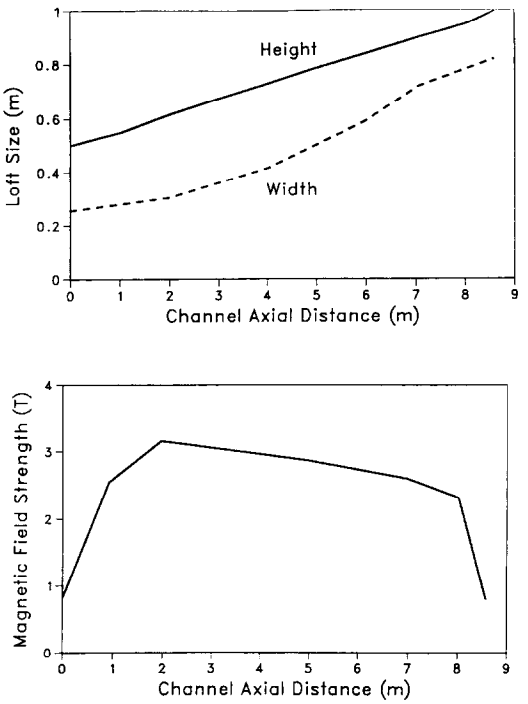

FIG. 4. Loft and magnetic field axial distributions for the AEDC channel.

applied to the three-dimensional Faraday generator model is emphasized in the following sections.

6.1. *Supersonic Faraday generator: the AEDC channel (test 14)*

The commercial-scale MHD Faraday generator of the High-Performance Demonstration Experiment (test 14) [22, 23] of the Arnold Engineering Development Center (AEDC) was simulated using the MGMHD computer code. In this test, the generator is operated in a supersonic mode and delivers an electrical power of about 23 MWe. The AEDC channel is approximately 8.9 m long, with a magnet of 7 m active length that can deliver a peak magnetic field of 3.2 T. The rectangular channel cross-section is non-uniform with a 0.49 m × 0.26 m cross-section at the channel inlet and a 0.99 m × 0.82 m cross-section at the exit. Figure 4 shows the axial distributions of the height and width of the channel and the magnetic field strength.

The channel contains 472 electrode pairs with variable electrode pitch. The first loaded electrode is located 0.82 m from the channel entrance. There is almost constant resistive loading parameter (resistance × electrode pitch) of about 0.8 Ω·m along the channel up to $Z = 7.7$ m, and then the channel is gradually unloaded over the last 0.6 m to prevent unacceptable voltage gradients in the magnetic field fringe.

The channel wall temperature distribution is taken to be the distribution estimated by AEDC at the time $t = 5$ s, at which steady-state conditions and good experimental data were obtained. The AEDC-estimated surface temperature is 1200 K at the channel entrance, which drops rapidly to about 850 K at $Z = 1.5$ m and then gradually decreases to 600 K at the channel exit. The resistive loading was originally selected to give a low supersonic velocity over the entire channel length at a magnetic field strength of up to 4 T. The nominal distributions of the resistive loading parameter, the magnetic field, and the wall temperature along the channel are given in refs. [22, 23].

In the following discussion, a vertical plane of symmetry through the center of the channel is assumed. This assumption of symmetry is legitimate because the electrical potential and hydrodynamic equations admit the central vertical plane as a plane of symmetry and because the selected inlet and boundary conditions are assumed uniform. A grid of 28 × 12 computational nodes with three grid levels is used. The axial step size is 4 cm. The plasma enters the channel with the inlet conditions shown in Table 4.

Figure 5 shows the calculated development of the transverse channel cross-section velocities at four axial locations along the generator length. First, in the inlet region of the duct (0–2 m), the flow diverges outwardly from the core region to the walls.

The center of divergence is not at the center of the channel but rather about one-third from the top of the channel. As the flow progresses downstream, two vortex patterns in the left and right sides of the channel are created because symmetry is assumed. Further down the channel where magnetohydrodynamic interactions become weaker ($Z = 8$ m), the flow continues to expand toward the duct walls, keeping strong secondary velocities in the side-wall regions. The maximum secondary flow velocity is about 80 m s^{-1}, which represents about 7% of the inlet velocity. An axial cross-section of the flow development shows that the flow enters the channel uniformly and is accelerated in the core of the channel (Fig. 6).

The flow does not separate at the walls and is supersonic throughout the channel. The predicted axial flow velocity in the cathode region is larger than that in the anode region, as illustrated in Fig. 6. This translates into a prediction of a greater shear stress and thus of a greater skin friction coefficient in the cathode wall region if the skin friction coefficient is defined upon the inlet central axial velocity.

A more illustrative representation of the axial velocity distribution is shown in Fig. 7 by means of

Table 4. Inlet conditions for the AEDC Faraday generator

Mass flow rate (kg s^{-1})	49
Temperature (K)	2804
Pressure (bar)	2.56
Conductivity (S m^{-1})	10.20
Hall parameter	2.18
Axial velocity (m s^{-1})	1153
Mach number	1.21

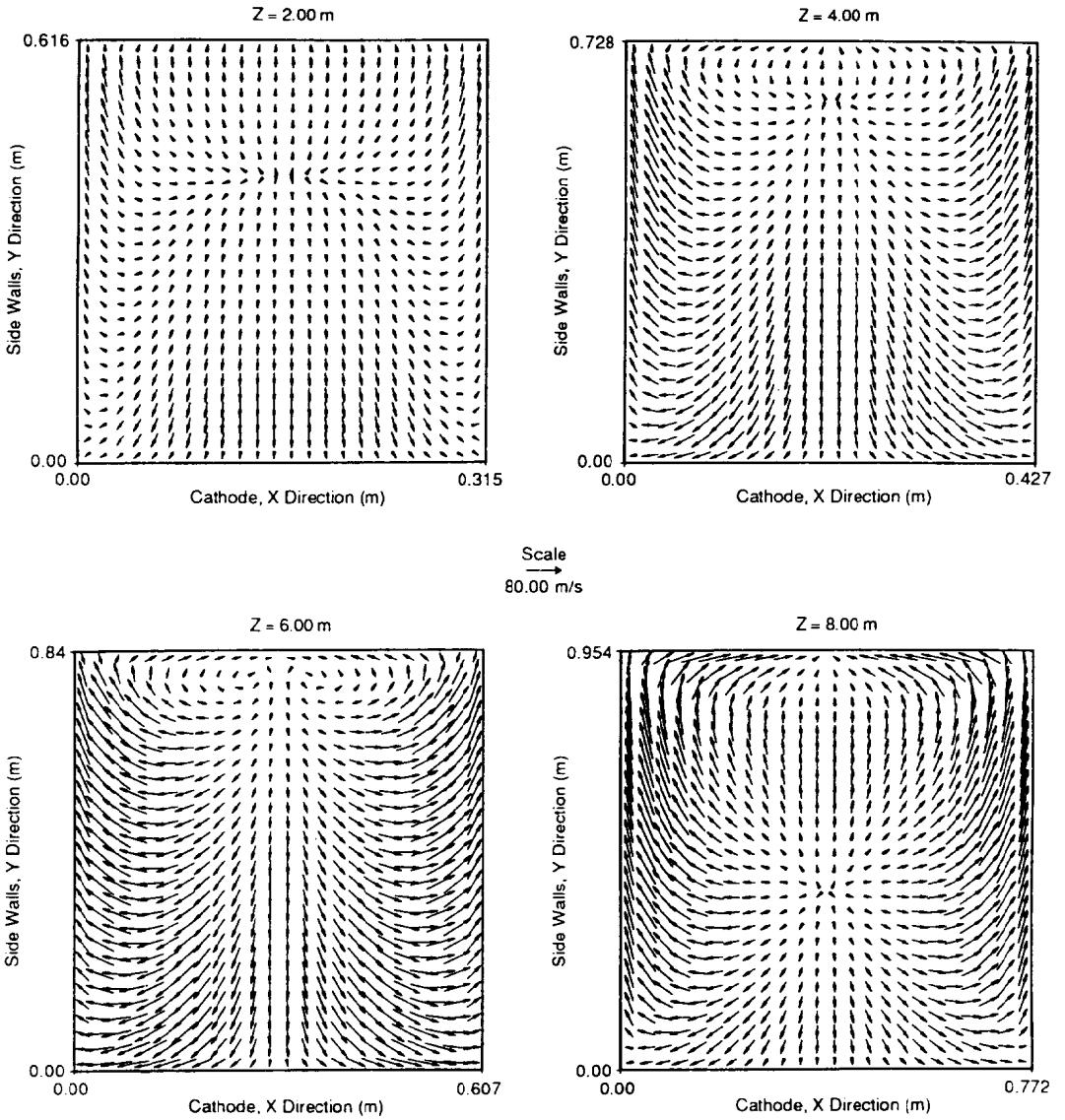

FIG. 5. Development of secondary flow vortices in the AEDC channel (test 14).

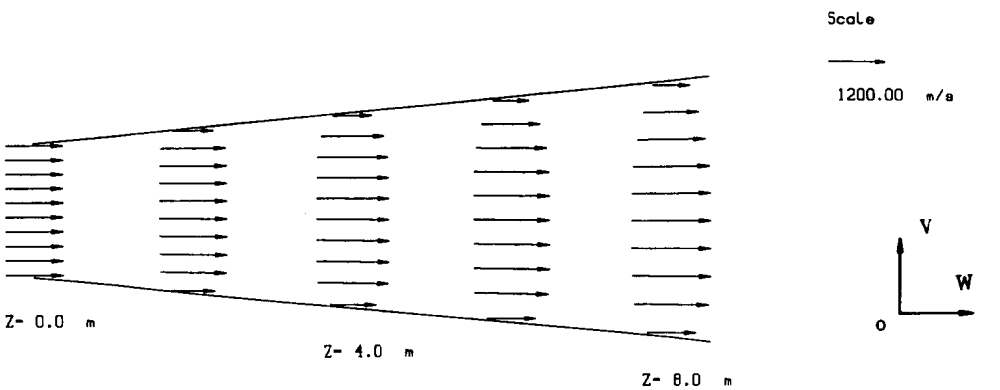

FIG. 6. Fluid flow in the central axial cross-section of the AEDC channel (test 14).

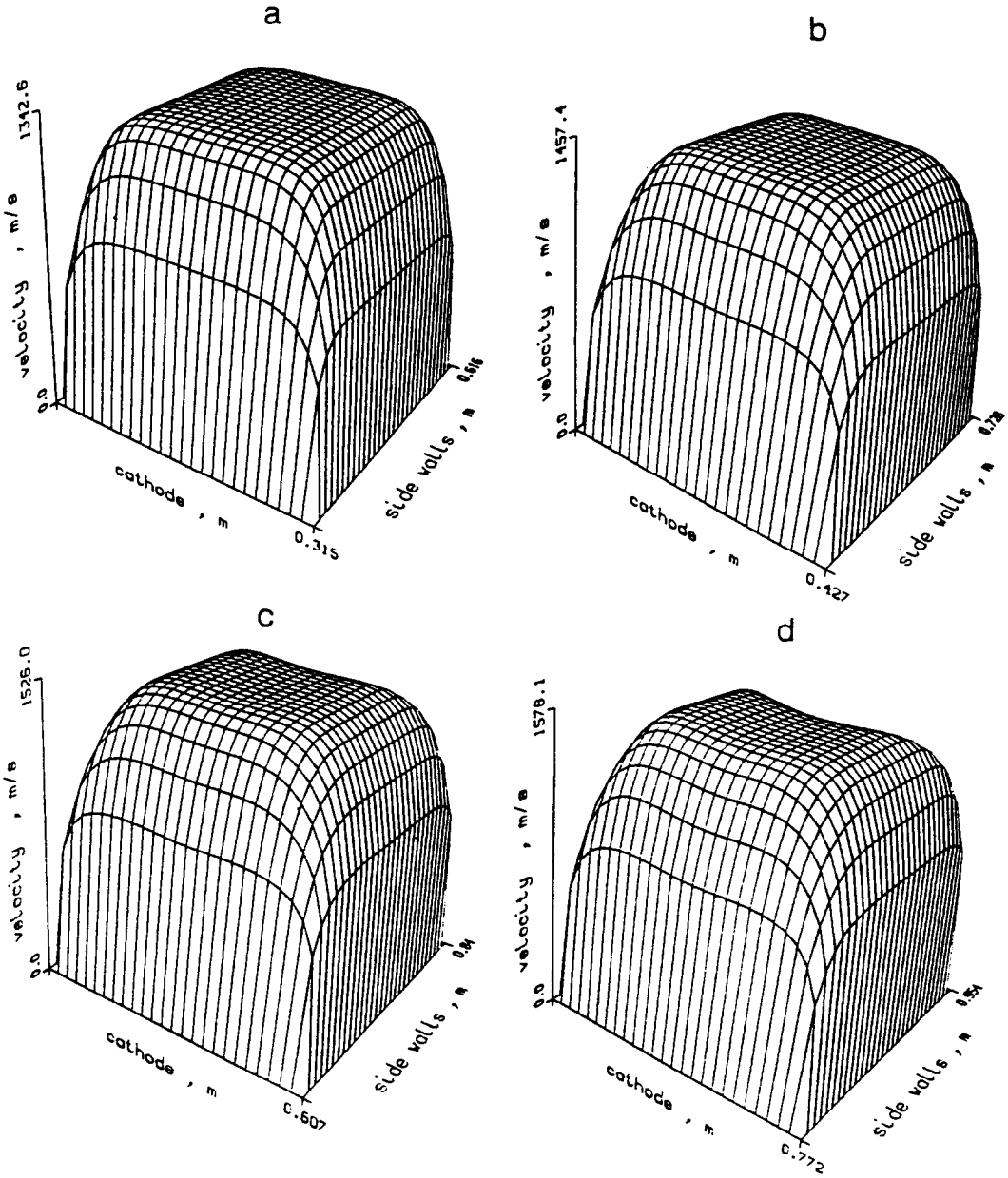

FIG. 7. Axial flow development in the AEDC Faraday channel (test 14) at an axial distance of: (a) 2 m, (b) 4 m, (c) 6 m, and (d) 8 m from channel inlet.

velocity surface plots. As can be seen, only small velocity overshoots are observed in the side-wall boundary layers, indicating that the strong secondary flows suppress any flow distortions that could develop in the transverse cross-section of the channel. Thus, strong secondary flows tend to establish uniform distributions of the axial velocity and temperature, which improve the global performance of the generator and limit the risks of MHD instabilities by current constrictions.

The predicted hydrodynamic and electrical performances of the AEDC test 14 were found to be in relatively good agreement with previously published predictions and experimental data, as can be seen in Fig. 8.

6.2. *Subsonic Faraday generator: the IEE MARK II generator*

The MARK II generator of the Institute of Electrical Engineering (IEE) facility is an experimental subsonic segmented 2 MWe Faraday generator designed for short-duration tests [24–27]. The generator is fired by combustion of diesel fuel in pure oxygen. As can be seen in Fig. 9, the axial pressure

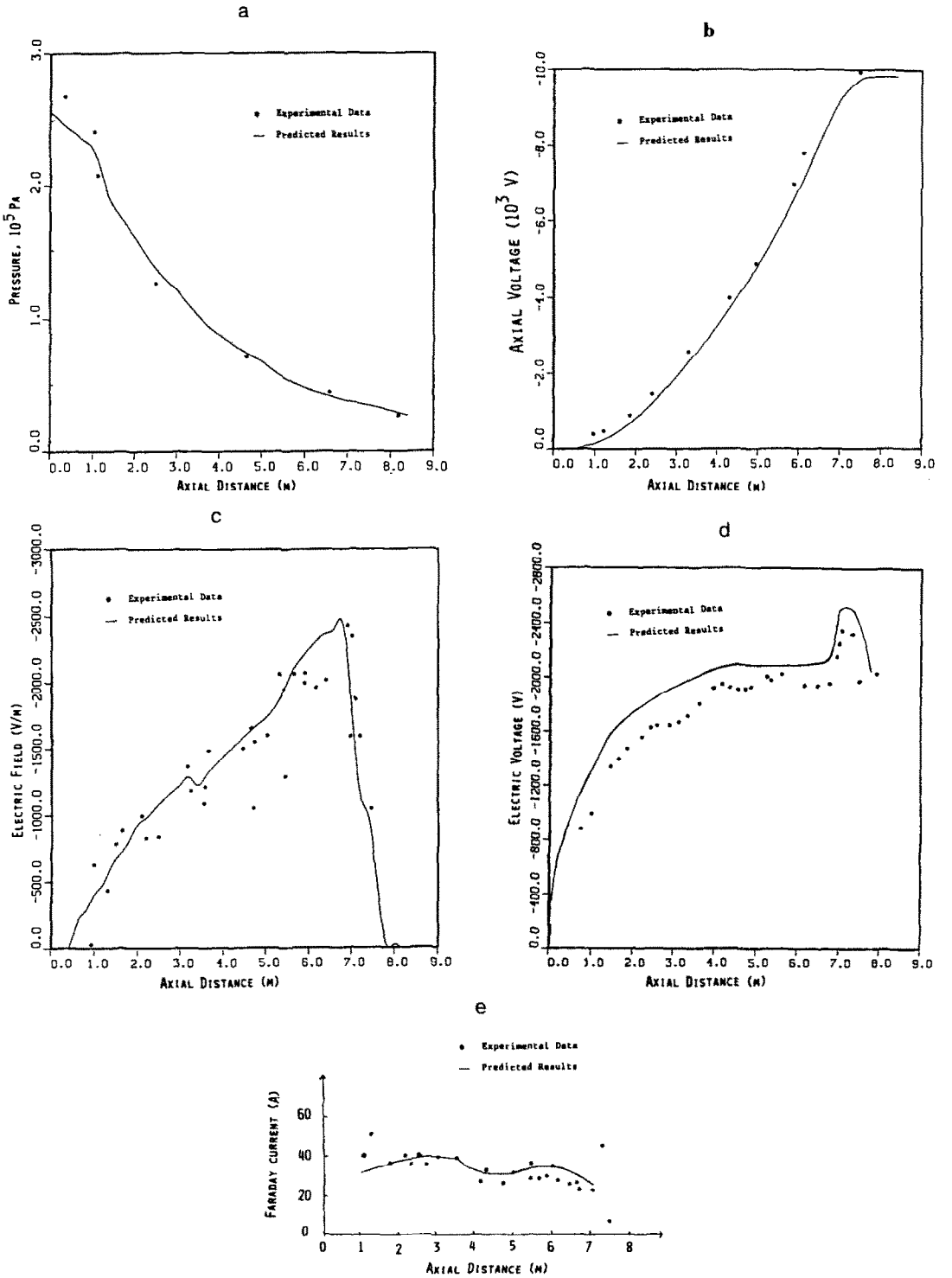

FIG. 8. Comparison of the axial distribution of: (a) pressure, (b) Hall voltage, (c) Hall electric field, (d) Faraday voltage and (e) Faraday current with experimental data for the supersonic Faraday generator (AEDC, test 14).

distribution compares well with experimental data. The channel is operated subsonically, and the plasma is mildly accelerating at the end of the channel active length. The predicted extracted electrical power (1.57 MWe) is in close agreement with that experimentally measured (1.60 MWe), as shown in Fig. 10 [24–27]. Further details regarding the comparison of the predicted and experimental results for the IEE MARK

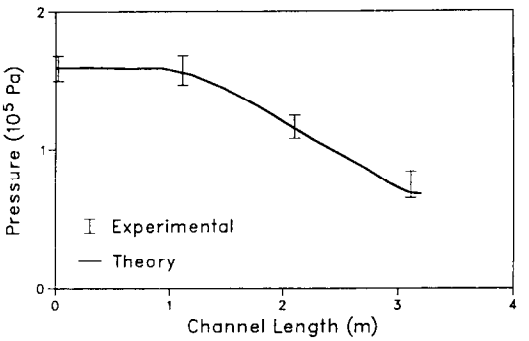

FIG. 9. Comparison of the predicted axial distribution of the pressure with experimental data for the MARK II subsonic Faraday generator.

II and AEDC generators can be found in Bouillard *et al.* [13, 28]. Due to space limitations, these details have been intentionally omitted in this paper; instead, the computational performances of the multigrid procedure have been emphasized in the following sections.

7. PROCEDURE COMPUTATIONAL PERFORMANCE

The performance of the multigrid (MGMHD) computer program was assessed and compared with that of the single-grid version (SGMHD) developed earlier by Vanka *et al.* [6]. The SGMHD computer code incorporates the same hydrodynamic and electrical models as described above. The SGMHD computer code also uses a similar marching technique in the flow direction, but, unlike MGMHD, it solves the uncoupled cross-sectional momentum and electrical equations using a single-grid alternating direction implicit (ADI) technique. In the following performance assessments and comparisons, the same plasma properties are used with both codes. The calculations were performed on an IBM PC-AT desktop computer equipped with a 32-bit coprocessor board.†

It is instructive to assess the performance of an algorithm by quantifying the workload of each individual task constituting the total calculation procedure. Such a task repartition is shown in Table 5 for several channel sections of the AEDC (test 14) generator. In this table, the global calculation procedure is first divided into five tasks: the multigrid solution of the cross-plane hydrodynamic and electrical equations, and the single-grid solution of the energy, axial momentum, and k–ε equations. Then, each multigrid task is subdivided into subtasks representing the work done on each individual grid. The CPU times of each task are expressed in terms of the number of fine-grid iterations and work units (WUs). In the multigrid procedure, a work unit is defined as the equivalent fine-grid iteration number required to perform a particular task. The computational work done on the coarser grids is expressed in terms of fine-grid iteration numbers (i.e. $\mathrm{WU} = \mathrm{NITER}^M + \mathrm{NITER}^{M-1}/4 + \mathrm{NITER}^{M-2}/4^2 + \ldots$ where NITER^k is the iteration number on grid k).

Table 5 displays the averaged computational workload of each task per axial step, which is calculated by averaging the total workload of each task for each section of the channel. The most expensive task is the electrical potential solution, which represents about 69% of the total computational workload. The multigrid computational work for the solution of the cross-plane momentum equations is relatively small and represents only about 2% of the total computation workload. Single-grid CPU time spent on the energy, axial momentum, and k–ε equations represents about 28% of the total computational workload. For the same problem (i.e. identical number of cells, cell size, and imposed residual errors), a typical breakdown of a single-grid procedure such as that used in SGMHD is shown in Table 6.

The solution of the single-grid electrical potential equation is by far the most expensive task and represents about 98% of the total computational workload. Note that the accuracy ($\mathrm{ERPOT} = 10^{-2}$) of the potential equations used in these calculations is somewhat high, and an accuracy ranging between 10^{-1} and 5×10^{-2} is usually suitable for most problems. Tables 5 and 6 show that for an imposed error of 10^{-2} on the potential equations, the MGMHD is about five times faster than a single-grid code, such as the SGMHD, for the test presented here.

A direct comparison of the convergence history of the potential residuals between the SGMHD and the MGMHD computer codes is presented in Fig. 11 for the first meter of the channel. This figure depicts the advantage of the multigrid technique as applied to the electrical potential equations (i.e. operator L of equation (13)).

The multigrid procedure allows a drastic reduction of the electric potential error—five orders of magnitude in less than 100 iterations (compared to 300

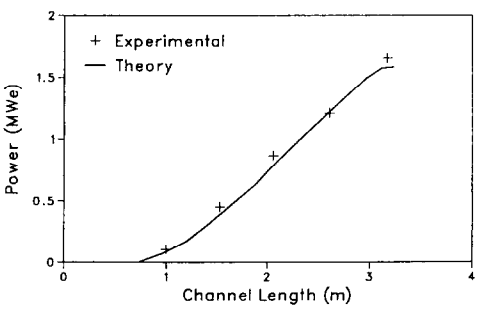

FIG. 10. Comparison of the predicted axial distribution of the electrical power with experimental data for the MARK II subsonic Faraday generator.

† DSI-750+/4 Megabytes, 32-bit coprocessor implemented on a PC-AT. Definicon Systems Inc. and Westlake Village and CA 91362.

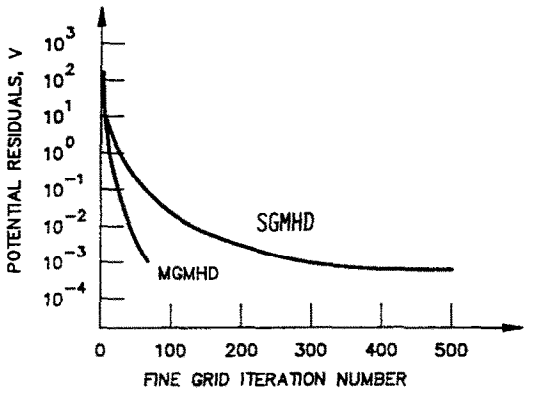

FIG. 11. Comparison of rates of convergence for the electrical potential solution between the single-grid (SGMHD) and multigrid (MGMHD) computer codes (12×28 nodes, axial step size $\Delta z = 0.04$ m).

iterations needed with SGMHD). Figure 11 provides a quick assessment of the computational performance of the multigrid procedure. For example, at an error residual of 2×10^{-2}, the computational speed using a multigrid solution technique is improved by a factor of 3, which is also reflected in the total CPU execution time shown in Table 7.

Table 7. Comparison of CPU time between the multigrid and the single-grid techniques for a Faraday channel simulation (for the total length of the channel)

ERPOT	Multigrid (min)†	Single-grid (min)†	Speed-up
10	Unstable	Unstable	—
1	Unstable	Unstable	—
0.1	34	65	2
0.02	50	150	3

† PC-AT CPU time.

8. CONCLUSIONS

A new multigrid, three-dimensional solution procedure was developed and illustrated by simulations of supersonic (AEDC) and subsonic (MARK II) Faraday generators. Validated with previously published predictions and experimental data, this new procedure performs about three to five times faster than the standard single-grid solution procedure. With the multigrid procedure, more detailed three-dimensional channel calculations can readily be performed for design purposes. Although the MHD model presented in this paper is not a comprehensive model, the multigrid methodology described herein can easily be extended to incorporate new features

Table 5. Typical breakdown of the MGMHD procedure averaged computational workload per axial step for the AEDC Faraday channel simulation (ERPOT = 10^{-2}, ERCONT = 5×10^{-3}; 12×28 nodes, $\Delta z = 0.04$ m)

	Cross-plane potentials				Cross-plane momentum						
	Iterations on grid no.				Iterations on grid no.						
Channel length (m)	1	2	3	WU	1	2	3	WU	Energy (WU)	Axial momentum (WU)	k–ε (WU)
0.0–0.2	316	64	36	72	2	3	2	3	4	6	16
0.2–0.4	324	66	38	75	0	0	1	1	4	5	16
0.4–0.6	194	56	30	56	0	0	1	1	4	5	14
0.6–0.8	120	48	26	46	0	0	1	1	4	5	14
0.8–1.0	160	58	28	52	0	0	1	1	4	5	14
Average task totals				61				2	4	6	15
Total WU: 88											

Global PC-AT CPU time = 6 min.

Table 6. Typical breakdown of the SGMHD procedure averaged computational workload per axial step for the AEDC Faraday channel simulation (ERPOT = 10^{-2}, ERCONT = 5×10^{-3}; 12×28 nodes, $\Delta z = 0.04$ m

Channel length (m)	Cross-plane potentials	Cross-plane momentum	Energy	Axial momentum	k–ε
0.0–0.2	2564	9	6	7	18
0.2–0.4	2052	1	6	7	16
0.4–0.6	1202	1	5	6	14
0.6–0.8	640	4	5	6	14
0.8–1.0	724	1	5	6	14
Average WU per task	1437	4	6	7	16
Average WU			1470		

Global PC-AT CPU time = 33 min.

and/or new models. Such features could be the incorporation of power take-off regions at the inlet and the exit of the channel, requiring mixed boundary condition treatment for the electrical potential equations in regions of interest.

Acknowledgements—This work was supported by the U.S. Department of Energy, Pittsburgh Energy Technology Center, under contract W-31-109-Eng-38 for the Pittsburgh Energy Technology Center. The authors thank J. L. Krazinski and S. P. Vanka for their help, their suggestions, and comments. Mountain Energy State Energy, AVCO, Systems Analysis Incorporated, and the University of Tennessee Space Institute provided valuable comments and suggestions in the evaluation and review of the preliminary documentation and version of the multigrid computer code.

REFERENCES

1. C. D. Maxwell, D. M. Markham, S. T. Demetriades and D. A. Oliver, Coupled electrical and fluid calculations in the cross plane in linear MHD generators. *Symp. on Engineering Aspects of MHD*, Vol. 16, pp. VII.3.13–VII.3.20 (1977).
2. S. T. Demetriades, C. D. Maxwell and D. A. Oliver, Progress in analytical modeling of MHD generators II. *Symp. on Engineering Aspects of MHD*, pp. 21:3.1.1–3.1.20 (1983).
3. S. T. Demetriades, D. A. Oliver, T. F. Swean and C. D. Maxwell, On the magnetoaerothermal instability. 19th Aerospace Science Meeting, Paper No. AIAA-81-0248 (1981).
4. S. T. Demetriades and G. S. Argyropoulos, Progress in analytical modeling of MHD power generators. *Symp. on Engineering Aspects of MHD*, Vol. 11, pp. I.5.1–I.5.13 (1972).
5. S. P. Vanka and R. K. Ahluwalia, Three-dimensional flow and heat transfer development in MHD channels. 19th Aerospace Sciences Meeting, Paper No. AIAA-81-0247 (1981).
6. S. P. Vanka, R. K. Ahluwalia and E. D. Doss, Three-dimensional analysis of MHD generators and diffusers. Technical Report, Argonne National Laboratory, ANL/MHD-82-4 (March 1982).
7. B. L. Liu, J. T. Lineberry and H. J. Schmidt, Simplified three-dimensional fluid and electrodynamic calculations for an MHD loading analysis. *AIAA/ASME 3rd Joint Conf. on Thermophysics*, Paper No. AIAA-82-0921 (1982).
8. M. L. Mittal, H. R. Nataraja and V. G. Naidu, Fluid flow and heat transfer in the duct of an MHD power generator, *Int. J. Heat Mass Transfer* **30**, 527–537 (1987).
9. S. V. Patankar and D. B. Spalding, A calculation procedure for heat, mass and momentum transfer for three-dimensional parabolic flows, *Int. J. Heat Mass Transfer* **15**, 1787–1806 (1972).
10. S. V. Patankar and D. B. Spalding, *Heat and Mass Transfer in Boundary Layers*. Intertext Books, London (1975).
11. B. E. Launder and D. B. Spalding, The numerical computation of turbulent flows, *Comput. Meth. Appl. Mech. Engng* **3**, 269–289 (1974).
12. C. V. Jayatillaka, Resistance of laminar sublayer to heat and mass transfer in boundary layers, Ph.D. thesis, University of London (1965).
13. J. X. Bouillard, J. L. Krazinski, S. P. Vanka and G. F. Berry, *User's Manual for MGMHD: A Multigrid Three-Dimensional Computer Code for the Analysis of MHD Generators and Diffusers*. Argonne National Laboratory, ANL/MHD-89-01 (1989).
14. R. K. Ahluwalia, S. P. Vanka, K. H. Im and S. A. Zwick, Formulation and assessment of a cross-plane electrical model for magnetohydrodynamic channels, *J. Energy* **6**(5), 314–322 (1982).
15. S. A. Zwick, E. D. Doss, Y. C. Pan and S. E. Shamma, MHD channel electrical boundary layer theory and application, *J. Energy* **7**(2), 118–127 (1983).
16. S. P. Vanka and R. K. Ahluwalia, Coupled three-dimensional flow and electrical calculations for Faraday MHD generators, *J. Energy* **7**(1), 65–72 (1983).
17. R. K. Ahluwalia and S. P. Vanka, Secondary flow effects in diagonal MHD channels, *J. Energy* **7**(5), 387–388 (1983).
18. R. A. Sacks, H. K. Geyer, S. J. Grammel and E. D. Doss, Modified NASA-Lewis chemical equilibrium code for MHD applications, Technical Report, Argonne National Laboratory, ANL/MHD-79-15 (1979).
19. S. P. Vanka, Block-implicit multigrid solution of Navier–Stokes equations in primitive variables, *J. Comp. Phys.* **65**, 138–158 (1986).
20. S. P. Vanka, A calculation procedure for three-dimensional steady recirculating flows using multigrid methods, *Comput. Meth. Appl. Mech. Engng* **55**, 321–338 (1986).
21. A. Brandt, *Multigrid Techniques: Guide with Applications to Fluid Dynamics*. Von Karman Institute, Lecture Series (1984).
22. R. F. Starr, L. S. Christensen, G. W. Garrison and G. L. Whitehead, Preliminary Faraday performance of a large magnetohydrodynamic generator at high magnetic field, *J. Energy* **6**(3), 163–170 (1982).
23. R. F. Starr, L. S. Christensen, G. L. Whitehead, G. W. Garrison, B. L. Seiber and R. L. Lawry, Report on the MHD performance demonstration experiment for the period October 1, 1979 to September 30, 1980, AEDC Report for DOE, ET-2895-10. Technical Report, AEDC (October 1985).
24. J. T. Lineberry, Y. C. L. Wu and B. C. Winkleman, MHD generator tests at the IEE MARK II facility. *Symp. on Engineering Aspects of MHD*, Vol. 25, pp. 2.4.1–2.4.14 (1987).
25. J. T. Lineberry, B. C. Winkelman and Y. C. L. Wu, Results of IEE MARK II generator experiments UTSI-IEE cooperative MHD research. *Symp. on Engineering Aspects of MHD*, Vol. 26, pp. 4.5.1–4.5.13 (1988).
26. Z. Ju, J. T. Lineberry and Y. C. L. Wu, Projected performance characteristics for the MARK II MHD generator of the IEE. *Symp. on Engineering Aspects of MHD*, Vol. 23, pp. 338–357 (1985).
27. B. L. Liu, J. T. Lineberry, Y. C. L. Wu and H. J. Schmidt, Three-dimensional analysis of the IEE MARK II MHD generator electric power generation, Tsukuba, Ibaraki, Japan. *Ninth Int. Conf on Magnetohydrodynamics*, Vol. 1, pp. 313–322 (1988).
28. J. X. Bouillard, J. L. Krazinski, S. P. Vanka and G. F. Berry, Performance of a multi-grid three-dimensional mhd generator calculation procedure. *Symp. on Engineering Aspects of MHD*, Vol. 27, pp. 5.2.1–5.2.11 (1989).

PERFORMANCES D'UNE PROCEDURE DE CALCUL MULTIGRILLE TRIDIMENSIONNELLE POUR LES GENERATEURS MAGNETOHYDRODYNAMIQUES

Résumé—On décrit la formulation et l'évaluation d'une procédure récemment développée de calcul multigrille aux différences finies pour des écoulements magnétohydrodynamiques tridimensionnels (MHD). La procédure résout, en variables primitives, le système d'équations MHD paraboliséees permanentes qui est constitué des équations de continuité, d'impulsion, d'énergie, de l'énergie cinétique de turbulence, de dissipation de turbulence et des équations de Maxwell, en utilisant une technique multigrille, implicite de différences finies. Cette nouvelle technique est tout d'abord validée en comparant les résultats de la prévision avec des données expérimentales pour les générateurs de Faraday supersoniques et subsoniques. Les performances de cette technique sont estimées en termes de vitesse de calcul et de précision de la solution. On montre que la résolution des équations elliptiques de Maxwell est limitante du point de vue vitesse de calcul. Un facteur global d'amélioration de 3–5 est obtenu en utilisant la procédure multigrille de différences finies.

DIE LEISTUNGSFÄHIGKEIT EINES DREIDIMENSIONALEN MEHRFACHGITTER-VERFAHRENS ZUR BERECHNUNG MAGNETOHYDRODYNAMISCHER GENERATOREN

Zusammenfassung—Es wird die Formulierung und Auswertung eines kürzlich entwickelten Mehrfachgitter Finite-Differenzen-Verfahrens zur Berechnung von stationären dreidimensionalen magnetohydrodynamischen (MHD) Strömungen beschrieben. Der parabolisierte Satz stationärer Gleichungen für MHD, der aus der Massenbilanz, aus 3 Impulsgleichungen, der Energiegleichung sowie den Gleichungen für die turbulente kinetische Energie und die Dissipationsrate und den Maxwellgleichungen besteht, wird mit einfachen Variablen mit Hilfe der genannten Prozedur gelöst. Dabei kommt eine implizite Mehrfachgitter Finite-Differenzen-Methode unter Verwendung einer Näherungsspeicherungsweise zur Anwendung. Das neue Verfahren wird zuerst durch Vergleich der erzielten Ergebnisse mit Versuchsdaten von Über- und Unterschall Faraday-Generatoren validiert. Die Leistungsfähigkeit dieses Verfahrens wird dann hinsichtlich der Berechnungsgeschwindigkeit und der Genauigkeit bewertet. Es zeigt sich, daß die Auflösung der elliptischen elektrischen Maxwellgleichungen die Berechnungsgeschwindigkeit beschränkt. Durch Verwendung der Mehrfachgitter Finite-Differenzen Lösungsprozedur ergibt sich ein globaler Beschleunigungsfaktor von 3–5.

ЭФФЕКТИВНОСТЬ МНОГОСЕТОЧНОГО МЕТОДА РАСЧЕТА ГЕНЕРАТОРОВ ТРЕСМЕРНЫХ МАГНИТОГИДРОДИНАМИЧЕСКИХ ТЕЧЕНИЙ

Аннотация—Представлены формулировка и оценка недавно разработанного многосеточного конечно-разностного метода расчета стационарных трехмерных магнитогидродинамических (МГД) течений. С использованием неявного многосеточного конечно-разностного метода предложенная методика позволяет решить в простейших переменных систему параболических стационарных МГД уравнений, состоящую из уравнения неразрывности, трех уравнений импульса, уравнения энергии, уравнений турбулентной кинетической энергии и скорости диссипации, а также уравнений Максвелла. Новый метод сначала апробируется посредством сравнения расчетных результатов с экспериментальными данными для сверхзвуковых и дозвуковых генераторов Фарадея. Затем эффективность метода оценивается по скорости вычислений и точности решения. Показано, что разрешающая способность эллиптических уравнений Максвелла ограничивает скорость вычислений. С использованием предложенной методики решения получен коэффициент глобыльного уточнения, составляющий 3–5.